As-doped SnSe single crystals: Ambivalent doping and interaction with intrinsic defects

K. Cermak Sraitrova [1], J. Cizek [2], V. Holy, [3,4] J. Kasparova [1], T. Plechacek [1], V. Kucek, [1]
J. Navratil [1], A. Krejcova, [1] and C. Drasar [1,*]

[1] *University of Pardubice, Faculty of Chemical Technology, Studentska 573, 53210 Pardubice, Czech Republic*
[2] *Faculty of Mathematics and Physics, Charles University, V Holesovickach 2, 18000 Praha 8, Czech Republic*
[3] *Faculty of Mathematics and Physics, Charles University, Ke Karlovu 3, 121 16 Praha 2, Czech Republic*
[4] *Masaryk University, Department of Condensed Matter Physics, Kotlarska 2, 61137 Brno, Czech Republic*

(Received 5 February 2020; revised 12 November 2020; accepted 25 January 2021; published 9 February 2021)

We performed ambivalent doping study on single crystals of two sets, $SnSe_{1-x}As_x$ and $Sn_{1-x}As_xSe$, with the aim to explore the interaction of doping species with intrinsic defects. We found that As atoms substitute preferentially for Se atoms in both sets forming the extrinsic substitutional point defect As_{Se}. In the first set, As lowers the concentration of Sn vacancies, V_{Sn}, by an order of magnitude compared to undoped stoichiometric SnSe crystal. The remaining Sn vacancies are preferentially coordinated with As atoms. Importantly, a very low concentration of As led to healing process of hosting structure in terms of intrinsic point defects and eventual $SnSe_2$ inclusions. This is reflected in an increase of the Hall mobility and drop of the Hall concentration. In the second set, the concentration of Sn vacancies markedly increases upon doping in contrast to the first set. Additionally, the coordination of Sn vacancies by As atoms is less evident due to the high concentration of vacancies. The substitutional defect As_{Se} is a deep-level defect that produces no free carriers at room temperature. Moreover, the coupling of V_{Sn} to As_{Se} defects increases their activation energy. This results in an unprecedentedly low Hall concentration in SnSe which stays below 10^{16} cm^{-3} for $x = 0.0075$. The present study indicates that doping of SnSe is a rather complex process that generally includes a strong interaction of doping atoms with the hosting structure. On the other hand, such doping allows adjustment of the type and concentration of defects. The present study reveals a general tendency of point defects to clustering, which modifies the properties of point defects markedly.

DOI: 10.1103/PhysRevB.103.085203

I. INTRODUCTION

The use of thermoelectric (TE) materials is one of the methods for processing waste heat and generating green electricity. Thus, TE materials represent a very attractive and important research area for future technologies. The efficiency of these materials is given by the formula $ZT = S^2\sigma T/\kappa$. ZT is a so-called figure of merit that is dimensionless, and its upper limit is not determined. This figure of merit consists of the Seebeck coefficient S, electrical conductivity σ, absolute temperature T, and thermal conductivity κ [1]. These parameters are interconnected, e.g., through the carrier concentration and band-structure parameters.

Materials with $ZT \geqslant 1$ are considered promising for practical applications as TE materials. Unfortunately, these values are usually reached at temperatures above ~700 K [2–4]. Most TE materials become physically and chemically unstable at these temperatures, and their properties change upon thermal cycling. Thus, shifting the maxima of ZT towards lower temperatures is a common strategy.

One of the very promising materials that have appeared during the last few years for these applications is SnSe [5]. This material has been studied in both single-crystalline [5] and polycrystalline forms [6]. While SnSe single crystals have excellent TE properties at elevated temperatures [5], polycrystalline SnSe yields mediocre [6]. According to Ref. [7], this difficulty might be partially eliminated by removing the tin oxide on the surface of this material.

SnSe undergoes a displacive phase transition, and at ~810 K, this material transforms from the α phase (*Pnma*) to the β phase (*Cmcm*) [8,9]. The α phase is characterized by a complicated orthorhombic structure that is one of the prerequisites for its significantly low thermal conductivity [10,11]. The main problem in both doped and undoped SnSe is its stability at elevated temperatures, which is even more serious in polycrystalline SnSe [12]. Additionally, the long-term stability and stability upon cycling of this material are problematic. As we showed in our previous work [13], the temperature and kinetics of the preparation and measurements play a significant role in this material.

Many elements and compounds have been studied as potential dopants for improving the TE properties of SnSe, with mixed results. The majority of doping studies deal with p-type doping. To date, dopants such as Ag [12,14], alkali metals (e.g., Refs. [15–20]), Zn [21], Cu [22], Tl [23], and Cd [24] have been studied. According to band studies [25–27], n-type SnSe should have superior TE properties in comparison with p-type SnSe. However, it seems to be difficult to prepare n-type SnSe. Only a few studies deal with n-type doping, e.g.,

*cestmir.drasar@upce.cz

 ©2021 American Physical Society

material doped with Bi [28] or Br [29]. To date, a suitable and stable dopant for shifting the efficiency maximum to a lower temperature region has not been found [26].

Together with doping studies, native defects have been emphasized recently. The most discussed defects are Sn vacancies [30]. According to our results published in Ref. [13], these defects govern the temperature region up to ∼500 K. Above this temperature, the nature of the defects changes; the Sn vacancies disappear, and Se vacancies together with vacancy clusters of $V_{Sn} + nV_{Se}$ appear. This phenomenon shows that up to ∼500 K, SnSe prefers a Se-rich composition, while above this temperature, SnSe prefers a Se-poor composition, and particles of the $SnSe_2$ phase appear. Importantly, the vacancy clusters play an important role in the extraordinary TE efficiency of SnSe at high temperatures. Selenium interstitials are also discussed in Ref. [31]. Their presence might be another prerequisite for low thermal conductivity in SnSe. However, the formation energy of Se interstitials is well above 2 eV, which makes these defects unlikely to form [32]. Both of these defects would represent a great opportunity for doping of the material if only we knew a way to induce them in the material even at low temperatures and stabilize them. One method might include doping with formally electrically inactive elements, i.e., with elements of the same formal oxidation state as the element being substituted. This method can change the formation energy of native defects and shift their concentration [33]. The use of an element of an ambivalent nature (i.e., an element capable of substituting in both anion and cation sublattices) may be another method. Based on this assumption, we present a careful analysis (case study) of doping with As, which we assume can replace both Se and Sn in SnSe. This assumption is corroborated by the existence of both As_2Se_3 and SnAs compounds. Thus, we present two sets of single-crystal As-doped samples to introduce As to the Se- and Sn sublattices. A similar paper was published on polycrystalline materials [34].

Additionally, SnSe and its analog SnS have been explored as materials for photovoltaic applications with a high theoretical conversion efficiency [35]. However, the experimental efficiency is much lower due to the high concentration of defects (point defects and related extraneous phases, e.g., $SnSe_2$) [13,36]. Thus, a procedure leading to a minimum concentration of defects would bring these materials closer to the application stage. For both TE and photovoltaic (PV) applications, it is important to understand the doping process and the interaction of the dopant with the native defects, which we address in this paper.

II. EXPERIMENTAL METHOD

A. Crystal growth

As-doped single crystals (SCs) as well as a set of non-stoichiometric single crystals were grown using the free-melt crystallization method. Ampoules containing elemental Sn and Se (of 5N purity) and compound AsSn (synthesized) at the desired stoichiometry were evacuated ($p < 10^{-3}$ Pa) and sealed. Afterwards, the sealed ampoules were heated (1.7 K/min) in a furnace up to 1223 K and remained at this temperature for 6 h followed by slow cooling (0.1 K/min) to 293 K. Using this procedure, we obtained two sets of As-doped SnSe: $SnSe_{1-x}As_x$ ($x = 0$–0.01), denoted *A* set, and $Sn_{1-x}As_xSe$ ($x = 0$–0.01), denoted *C* set, and a set of undoped nonstoichiometric reference samples $Sn_{2-y}Se_y$ ($y = 0.99$–1.01). The phase purity was checked using powder x-ray diffraction (XRD) [37]. Optical atomic spectroscopy was used to obtain actual chemical composition of As-doped samples. The chemical analysis results are summarized in Supplemental Material [38].

B. Positron annihilation

A ^{22}Na radioisotope with an activity of ≈1 MBq was used as a positron source for positron annihilation spectroscopy (PAS). A carrier-free ^{22}NaCl radioisotope was sealed between two Mylar foils with a thickness of 2 μm. Two complementary PAS techniques were employed: (i) positron lifetime (LT) spectroscopy, providing information about the type and concentration of open volume defects [39], and (ii) coincidence Doppler broadening (CDB) [40], which probes the local chemical environment of defects. PAS measurements were carried out at room temperature.

A digital spectrometer [41] with a time resolution of 145 ps [full width at half maximum (FWHM) of the resolution function] was employed for LT measurements. At least 10^7 positron annihilation events were accumulated in each LT spectrum. Decomposition of the LT spectra into individual exponential components was performed using a maximum-likelihood code [42]. The source contribution to the LT spectra consisted of (i) a component with lifetime of ≈368 ps and relative intensity of ≈11% representing a contribution of positrons annihilated in the source spot and inside the Mylar foil, and (ii) a weak long-lived component with lifetime of ≈1.5 ns and intensity of ≈1% originating from pick-off annihilation of ortho-positronium formed in the covering Mylar foil. The source contribution was determined by measuring of a reference sample of well-annealed Fe and its intensity has been recalculated for SnSe according to the formula published in Ref. [43]. The CDB studies were carried out using a digital spectrometer [44] equipped with two high-purity Ge detectors. The CDB spectrometer was characterized by an energy resolution of 0.9 keV at the annihilation line and a peak-to-background ratio higher than 10^5. The two-dimensional CDB spectrum of each sample contained at least 10^8 annihilation events. The results of the CDB measurements are presented in this paper as ratio curves related to a well-annealed pure Al (99.9999%) reference sample.

C. Calculations of positron annihilation parameters

Density-functional theory (DFT) was employed for calculations of the positron annihilation-related parameters such as the positron lifetime using the atomic superposition (ATSUP) method [45] which retains the true three-dimensional geometry of the crystal lattice but the electronic structure is not self-consistent. The ATSUP method is computationally very effective when compared to the methods using self-consistent electron densities and enables calculation of positron density in large supercells required for modeling of isolated point defects. The positron annihilation in the SnSe crystal was

calculated within the so-called standard scheme [46], which assumes that the positron density is vanishingly small everywhere and does not affect the bulk electron structure. The electron density $n(\boldsymbol{r})$ in the material was calculated first without the presence of positrons by superimposing atomic densities calculated by a relativistic Dirac-Fock code [47,48]. Subsequently, the effective potential for a positron was constructed as

$$V_+(\boldsymbol{r}) = \phi(\boldsymbol{r}) + V_{\text{corr}}[n, \nabla n], \quad (1)$$

where $\phi(\boldsymbol{r})$ is the Coulomb potential produced by the charge distribution of electrons and nuclei and V_{corr} is the electron-positron correlation potential in the limit of vanishing positron density [46].

The ground state of the positron wave function $\psi_+(\boldsymbol{r})$ and the energy E_+ were calculated by solving a single-particle Schrödinger equation

$$-\tfrac{1}{2}\nabla^2\psi_+(\boldsymbol{r}) + \mathrm{V}_+(\boldsymbol{r})\psi_+(\boldsymbol{r}) = E_+\psi_+(\boldsymbol{r}). \quad (2)$$

The Schrödinger equation was solved on a three-dimensional real-space mesh using a finite-difference method [49]. The positron lifetime was determined by the overlap of the electron density $n(\boldsymbol{r})$ and the positron density $n_+(\boldsymbol{r}) = |\psi_+(\boldsymbol{r})|^2$

$$\tau = \left\{\pi r_e^2 c \int n_+(\boldsymbol{r}) n(\boldsymbol{r}) \gamma[n, \nabla n] d\boldsymbol{r}\right\}^{-1}, \quad (3)$$

where r_e is the classic electron radius and c is the speed of light. The enhancement in the electron density at the site of the positron due to positron-electron correlation was considered through the enhancement factor γ [46], which was treated within two different approaches:

(i) local density approximation (LDA) using the parametrization by Boronski and Nieminen [50] with a correction for incomplete positron screening in semiconductors [51] assuming a high-frequency dielectric constant of $\varepsilon_\infty = 15$ [52]. Within this approach the enhancement factor and electron-positron correlation potential are determined by the electron density n in the site of positron;

(ii) the generalized gradient approximation (GGA) scheme developed by Barbiellini *et al.* [53]. Within this approach, the enhancement factor γ and the electron-positron correlation potential V_{corr} were determined by the local electron density n and its gradient ∇n at the positron annihilation site.

The LDA approach overestimates positron annihilation rates especially with d electrons [30] and calculated lifetimes are usually slightly shorter than experimental values. The GGA scheme usually yields higher positron lifetimes compared to LDA; in some systems it may overestimate the experimental lifetime value [35]. Since positron lifetimes obtained using LDA and GGA approach differ, the comparison of calculated lifetimes with experiment is not straightforward. For the sake of comparison with experiment the calculated lifetime values τ were divided by the bulk positron lifetime τ_{B} calculated within the same approach (i.e., LDA or GGA). The lifetime ratios τ/τ_{B} calculated within LDA and GGA are rather similar [54] and can be compared with experimental values.

The momentum distribution of annihilating electron-positron pairs was calculated using the approach described in Refs. [55,56]. Electrons belonging to a shell of ith atom described by the principal quantum number n and the angular quantum number l contribute to the momentum distribution by

$$\rho^{i,nl}(p) = 4\pi^2 r_e^2 c N^{i,nl} \gamma^{i,nl} \left| \int R_+^i R_-^{i,nl} B_l(pr) r^2 dr \right|^2, \quad (4)$$

where $N^{i,nl}$ is the number of electrons in the shell, B_1 is the spherical Bessel function, and R_+^i and $R_-^{i,nl}$ denote the radial parts of the positron and electron wave functions, respectively. The symbol $\gamma^{i,nl}$ stands for the state-dependent positron enhancement factor [56]. The total momentum distribution of the annihilating electron-positron pairs was obtained by summing the partial contributions $\rho^{i,nl}(p)$ of the electron shells of all the occupied atomic sites. To account for the finite energy resolution of the CDB spectrometer, the calculated momentum distributions were convoluted with a Gaussian function with a FWHM of 3.5×10^3 m_0c.

The present approach describes the high-momentum part ($p > 10 \times 10^{-3}$ m_0c) of the momentum distribution of the annihilating pair well, with a dominating contribution from core electrons that retain their atomic character and are almost not influenced by crystal bonding. The calculated momentum distributions are presented as ratio curves related to pure Al, which means that the calculated momentum distributions were divided by the momentum distribution calculated for a perfect (defect-free) Al crystal. This enables comparison of the calculated curves with the results from experiments in the high-momentum range where the contribution of positrons annihilated by core electrons dominates. Core electrons located in inner shells retain their atomic character and are almost unaffected by crystal bonding.

Theoretical calculations were performed using 512 atom-based supercells of the *Pnma* SnSe phase with an orthorhombic structure ($a = 11.492$ Å, $b = 4.151$ Å, $c = 4.442$ Å) [9], which represents the thermodynamic equilibrium phase at temperatures below ≈800 K [57,58]. A Brillouin-zone integration over the lowest-lying positron state described in Ref. [54] was used in the calculations of the positron parameters for point defects to achieve a rapid convergence of the results with respect to the supercell size. Vacancies (V_{Se} or V_{Sn}) and their complexes with As were modeled by removing Se or Sn and adding the corresponding number of As ions to the supercell. Ion relaxation around vacancies has not been considered in the present state of calculations. Note that a positron localized in a vacancy influences positions of ions surrounding the vacancy. Positron-induced forces cause usually an outward relaxation of the neighboring ions. It has been shown that positron-induced outward relaxation is higher in magnitude than the inward relaxation of ions without the presence of a positron [59]. Hence, in order to determine positron lifetime for a relaxed defect it is necessary not only to determine the relaxed geometry of defect without a positron, but also to consider relaxations caused by positron-induced forces. Such demanding calculations are out of the scope of this work but represent a challenge for future theoretical approach. Thus, shortening of positron lifetime due to (usually)

TABLE I. Lifetimes (LTs) for various positron states in SnSe (*Pnma*) obtained from calculations using the LDA and GGA approach for electron-positron correlations. Ratios of calculated LTs τ to the bulk lifetime τ_B calculated using the same approach are listed in the table as well.

	LDA		GGA	
State	τ (ps)	τ/τ_B	τ (ps)	τ/τ_B
Bulk	206	1	217	1
V_{Sn}	278	1.35	308	1.42
V_{Se}	258	1.25	279	1.29
$V_{Sn} + V_{Se}$	313	1.52	358	1.65
$2V_{Sn}$	281	1.37	317	1.46
$V_{Sn} + 2V_{Se}$	338	1.64	396	1.82
$V_{Sn} + 3V_{Se}$	358	1.74	431	1.98
$As_{Se} + V_{Sn}$	278	1.35	307	1.41
$As_{Se} + 2V_{Sn}$	281	1.37	315	1.45
$As_{Se} + 3V_{Sn}$	285	1.39	322	1.48
$As_{Se} + 4V_{Sn}$	289	1.41	331	1.52
$As_{Sn} + V_{Se}$	264	1.29	284	1.31
$As_{Sn} + 2V_{Se}$	277	1.35	301	1.38
$As_{Sn} + 3V_{Se}$	288	1.40	314	1.45
$V_{Sn} + As_{Se} + V_{Se}$	314	1.53	357	1.64

inward relaxation of neighboring ions and its prolongation due to (usually) outward displacement caused by positron-induced forces cancel to some extent each other and positron lifetimes calculated for nonrelaxed defects are often in better agreement with experiment than lifetimes calculated for relaxed defects but neglecting the effect of positron-induced forces [59,60].

D. Transport measurements

All of the transport parameters were obtained within the temperature range from 80 to 480 K. The electrical conductivity $\sigma(i \parallel b)$ and Hall coefficient $R_H(i \parallel b; B \parallel a)$ were measured simultaneously via a lock-in nanovoltmeter with a 29-Hz excitation. A static magnetic field of 0.6 T was also used for the R_H measurements. Due to the very high resistivity of the As-doped and nonstoichiometric samples, all of the leads were attached to the samples using the conductive graphite adhesive Aquadag. The hole concentration was determined using the equation $R_H = 1/he$. The longitudinal steady-state technique was used for the measurement of the Seebeck coefficient $S(\Delta T \parallel b)$. The temperature gradient oscillated from 3 to 3.5 K and was determined by copper-constantan thermocouples.

III. RESULTS AND DISCUSSION

A. Positron annihilation spectroscopy

Table I shows the LTs calculated for various positron states. The calculated bulk positron lifetime, i.e., the lifetime of free positrons delocalized in a perfect (defect-free) lattice of the *Pnma* phase of SnSe, is $\tau_B = 206$ and 217 ps for LDA and GGA approach, respectively. Ratios τ/τ_B of calculated LTs and the bulk lifetime calculated using the same approach are listed in the table as well. Both Sn vacancies (V_{Sn}) and Se vacancies (V_{Se}) represent deep trapping sites for positrons,

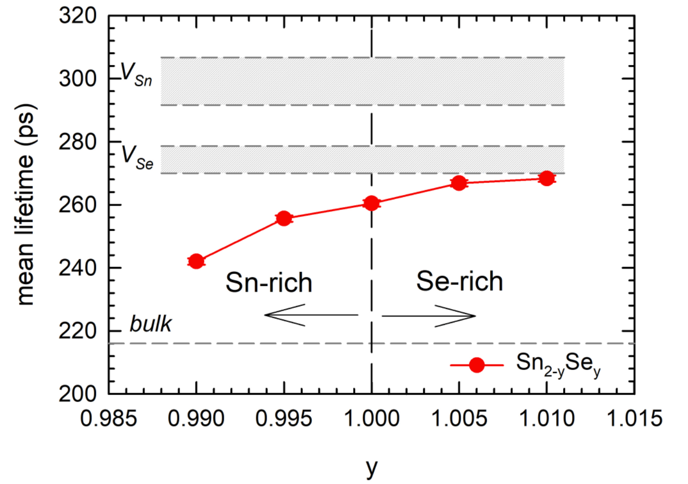

FIG. 1. The development of the mean positron lifetime for binary $Sn_{2-y}Se_y$ SCs. Hatched bands indicate intervals of τ/τ_B values calculated using the LDA and GGA approach and scaled by $\tau_{B,exp}$.

characterized by positron binding energies higher than 1 eV. V_{Sn} exhibits a larger open volume than V_{Se}, which is reflected by a longer lifetime for positrons trapped in V_{Sn} ($\tau/\tau_B \approx 1.4$) than for positrons trapped in V_{Se} ($\tau/\tau_B \approx 1.3$). Two types of V_{Se} exist in the *Pnma* phase. However, the difference between the calculated lifetimes of the positrons trapped in the two types of V_{Se} does not exceed 0.5 ps and can be neglected. Table I also lists the calculated lifetimes for complex defects, i.e., complexes of V_{Sn} and V_{Se} with As substituting for Se (As_{Se}) or Sn (As_{Sn}) atoms for both $SnAs_xSe_{1-x}$ and $Sn_{1-x}As_xSe$ (*A*- and *C* sets). The calculated lifetime increases with increasing free volume for the defects.

Sets of binary samples $Sn_{2-y}Se_y$ ($y = 0.99$–1.01) SCs with slightly varied stoichiometry have been studied for comparison in order to examine the effect of nonstoichiometry on the formation of point defects. Figure 1 shows the development of the mean positron lifetime $\tau_{mean} = \sum_i \tau_i I_i$ with the Se concentration y. The mean positron lifetime is a robust parameter that is not affected by mutual correlations between the fitting parameters. Hence, the behavior of τ_{mean} provides good insight into the development of defects in SnSe SCs. The stoichiometric SnSe exhibits the mean lifetime $\tau_{mean} \approx$ 260 ps. For Se-rich samples ($y > 1$) τ_{mean} further increases, while in Sn-rich samples ($y < 1$) τ_{mean} decreases.

Results of decomposition of LT spectra of $Sn_{2-y}Se_y$ SCs are plotted in Fig. 2. LT spectra of all $Sn_{2-y}Se_y$ SCs studied can be well described by two exponential components (except of the source contribution). The development of lifetimes τ_1 and τ_2 of these components with composition y are plotted in Fig. 2(a) while Fig. 2(b) shows corresponding intensities. The shorter component with lifetime τ_1, which is lower than the calculated bulk positron lifetime for SnSe, can be attributed to free positrons while the longer component with lifetime τ_2 represents a contribution of positrons trapped in defects.

Assuming that positrons are trapped at uniformly distributed defects and that positron binding energy is high enough so that positron detrapping is negligible, the LT spectra can be described using the two-state simple trapping model (STM) [61]. Within the STM, the parameters of the

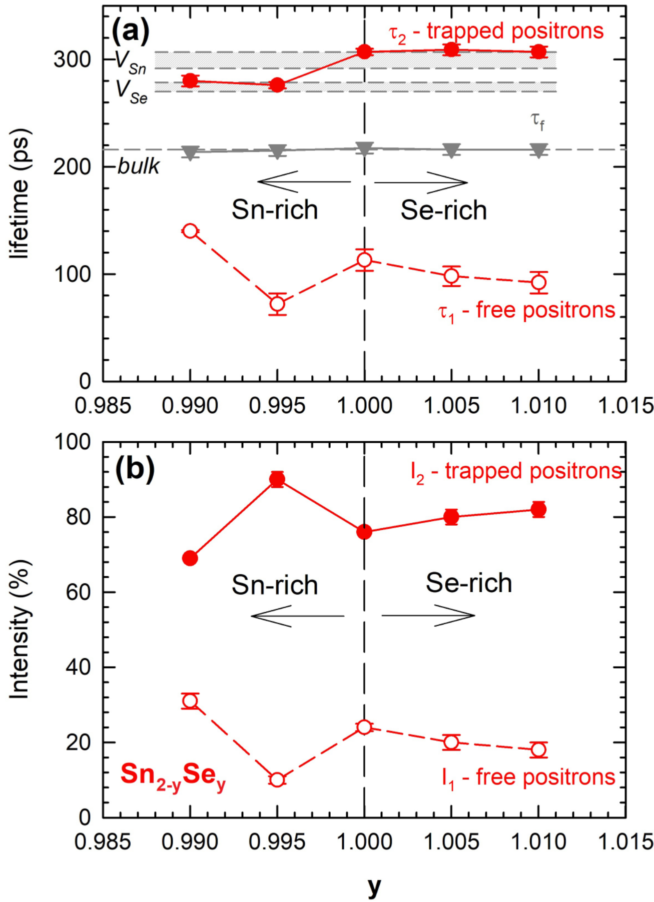

FIG. 2. Results of LT investigations of $Sn_{2-y}Se_y$ SCs: (a) development of lifetimes τ_1, τ_2 resolved in LT spectra; (b) behavior of corresponding relative intensities. The quantity τ_f calculated using STM is plotted in panel (a) as well. Hatched bands indicate τ/τ_B values calculated for V_{Se} and V_{Sn} and scaled by $\tau_{B,exp}$.

exponential components τ_i and I_i are not fully independent but are interconnected so that the quantity

$$\tau_f = \left\{ \sum_i \frac{I_i}{\tau_i} \right\}^{-1} \tag{5}$$

always equals the bulk positron lifetime, i.e., the lifetime of the free positrons delocalized in a perfect SnSe lattice: $\tau_f = \tau_B$ We can see in Fig. 2 that the quantity τ_f calculated using Eq. (5) and plotted by gray triangles remains approximately constant for all $Sn_{2-y}Se_y$ SCs. The average τ_f value of (216 ± 1) ps agrees well with the SnSe bulk lifetime calculated using the GGA approach. Hence, one can conclude that assumptions of the STM are fulfilled in the set of $Sn_{2-y}Se_y$ SCs and the experimental SnSe bulk lifetime value can be estimated as $\tau_{B,exp} = (216 \pm 1)$ ps. This value will be used as the bulk lifetime of SnSe in the further analysis in the present paper.

The calculated lifetime ratios τ/τ_B can be now scaled by multiplying with $\tau_{B,exp}$ to get absolute values of lifetimes which can be directly compared with experiment. The lifetime values for free positrons delocalized in a perfect SnSe lattice (bulk) and positrons trapped in V_{Sn} and V_{Se} obtained by this approach are shown by hatched bands in Figs. 1 and 2(a).

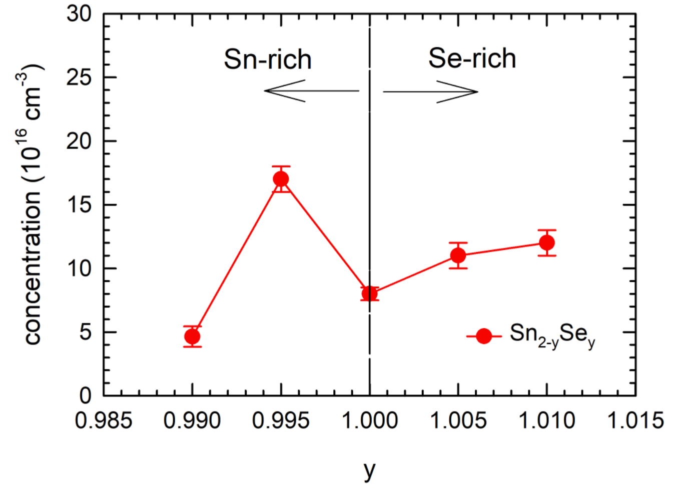

FIG. 3. The concentrations of point defects detected by LT spectroscopy in binary $Sn_{2-y}Se_y$ SCs, namely V_{Sn} for Se-rich and V_{Se} for Sn-rich samples.

From inspection of Fig. 2(a) one can conclude that Se-rich $(y > 1)$ samples exhibit higher lifetime τ_2 which is comparable with the value $\tau/\tau_B \approx 1.4$ calculated for V_{Sn}. On the other hand, Sn-rich samples exhibit lower τ_2 value comparable with $\tau/\tau_B \approx 1.3$ calculated for V_{Se}. Hence, one can conclude that Se-rich crystals contain V_{Sn} and the stoichiometric sample SnSe contains V_{Sn} as well [13]. However, for Sn-rich crystals the nature of defects changes and Sn-rich samples contain V_{Se} as dominating type defects.

The concentration of defects can be calculated within STM from the following equation [61]:

$$c_i = \frac{I_i}{\nu_i}\left(\frac{1}{\tau_1} - \frac{1}{\tau_i}\right), \tag{6}$$

where ν_i is the trapping coefficient (cross section of positron trapping per unit concentration of the defect) for the corresponding type of defect [39]. Since the exact values of the trapping coefficient for the vacancies in SnSe are unknown for V_{Se} and V_{Sn}, we use $n_V = 10^{15}$ at s^{-1}, representing an order of magnitude estimation of ν_i for neutral monovacancies in semiconductors [39]. The concentrations of vacancies in $Sn_{2-y}Se_y$ SCs calculated using Eq. (6) are plotted in Fig. 3.

The results of the LT investigations of As-doped samples are summarized in Figs. 4–7. Figure 4 shows the trend of mean lifetime τ_{mean} with the content of As in the samples. The behavior of τ_{mean} is markedly different for the *A*- and *C* sets. The τ_{mean} decreases in $SnAs_xSe_{1-x}$ (*A* set) with increasing As concentration, approaching the defect-free bulk lifetime. This result indicates that the fraction of positrons annihilating in the trapped states gradually decreases with As content. The lowest concentration of defects occurs at approximately $x = 0.005$ for the *A* set, which reflects the off-stoichiometry of formally stoichiometric SnSe (Fig. 3). In contrast, for $Sn_{1-x}As_xSe$ (*C* set), the mean lifetime increases to longer than 300 ps, indicating that annihilation occurs mostly in trapped states in open volume defects as the As content increases.

The decomposition of the LT spectra into individual components provides deeper insight into the development of

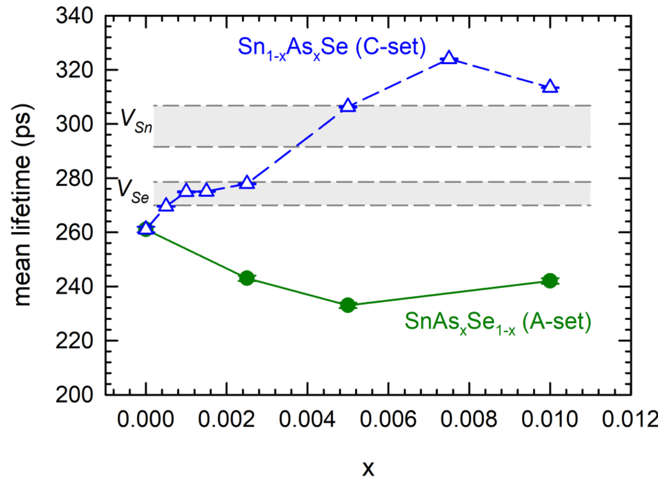

FIG. 4. The mean positron lifetime τ_{mean} plotted as a function of the concentration of As dopant (x) in $SnAs_xSe_{1-x}$ (A set) and $Sn_{1-x}As_xSe$ (C set). Hatched bands show region of τ/τ_B values calculated for monovacancies V_{Se} and V_{Sn} and scaled by $\tau_{B,\exp}$.

defects in As-doped SnSe samples. Figure 5 shows the lifetimes τ_i of the exponential components resolved in the LT spectra as a function of As content x in the A- and C sets. For $SnAs_xSe_{1-x}$ [Fig. 5(a)], the lifetime τ_1 of the free positron component approaches the bulk lifetime $\tau_B = 216$ ps (i.e., the lifetime of free positrons in a perfect SnSe lattice) with increasing As content due to extinction of V_{Sn}, which is the dominant defect in undoped SnSe at room temperature [13]. The lifetime τ_2 of trapped positrons is approximately 307 ps, and for increased As content $x = 0.01$, the lifetime increases to $\approx$315 ps. For $Sn_{1-x}As_xSe$ [Fig. 5(b)], the lifetime τ_1 of the free positron component decreases with increasing As content, indicating enhanced positron trapping. The lifetime τ_2 of trapped positrons is approximately 320 ps.

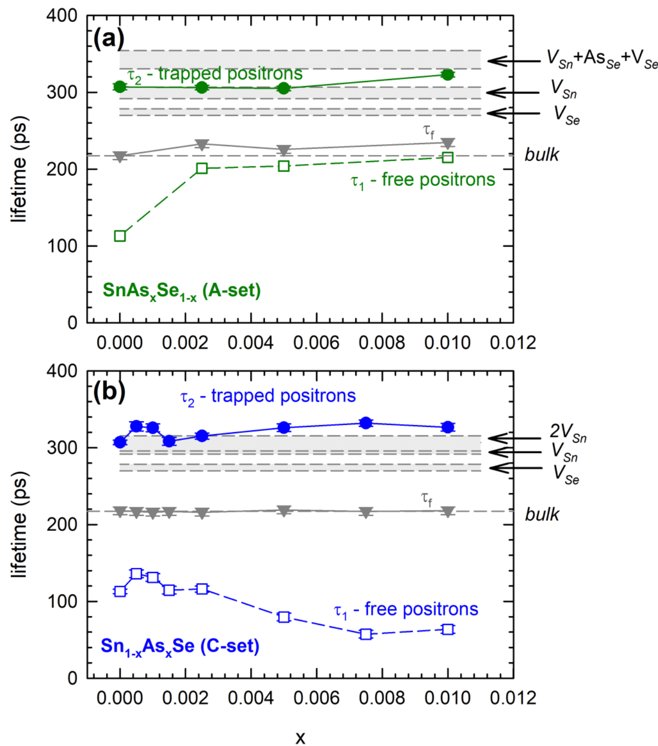

FIG. 5. The development of the lifetimes τ_i of the exponential components resolved in the LT spectra as a function of As content: (a) $SnAs_xSe_{1-x}$ (A set); (b) $Sn_{1-x}As_xSe$ (C set). The quantity τ_f calculated using Eq. (5) is also plotted in the figure. Hatched bands indicate calculated lifetime ratios τ/τ_B for various positron states multiplied by $\tau_{B,\exp}$.

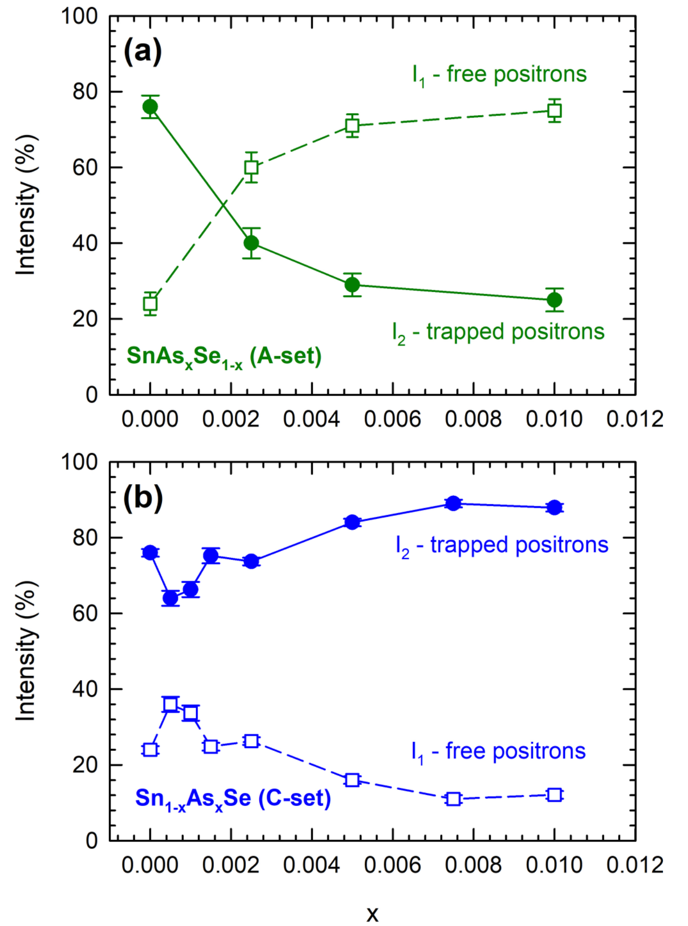

FIG. 6. The development of the intensities I_i of the exponential components resolved in the LT spectra as a function of the As content: (a) $SnAs_xSe_{1-x}$ (A set); (b) $Sn_{1-x}As_xSe$ (C set). Note that the intensities are normalized so that $\sum_i I_i = 100\%$.

The trend of the corresponding intensities I_i of the components resolved in the LT spectra is plotted in Fig. 6 as a function of x. From the intensities, we can conclude that the concentration of positron traps decreases with As content for the A set, while the opposite applies for the C set. Figure 7 shows calculated τ/τ_B ratios of positrons trapped in V_{Sn} and V_{Se} associated with various numbers of As ions in the nearest-neighbor (NN) sites. Inspection of the figure shows that the LT of positrons trapped in V_{Se} exhibits a pronounced increase with increasing number of As_{Sn} NNs. On the other hand, the LT of positrons trapped in V_{Sn} remains approximately constant (LDA data) or slightly decreases (GGA data) with increasing number of As_{Se} ions up to 6 NNs. For the $V_{Sn} + 7As_{Sn}$ complex, LT increases again.

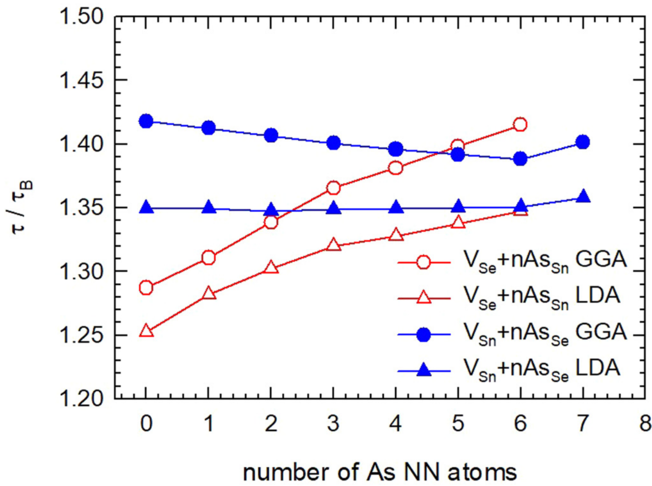

FIG. 7. The development of the lifetime ratio τ_i/τ_B calculated using LDA and GGA approach for positron-electron correlation for V_{Se} and V_{Sn} as a function of the number of As ions As_{Sn} and As_{Se} in the NN sites surrounding vacancies.

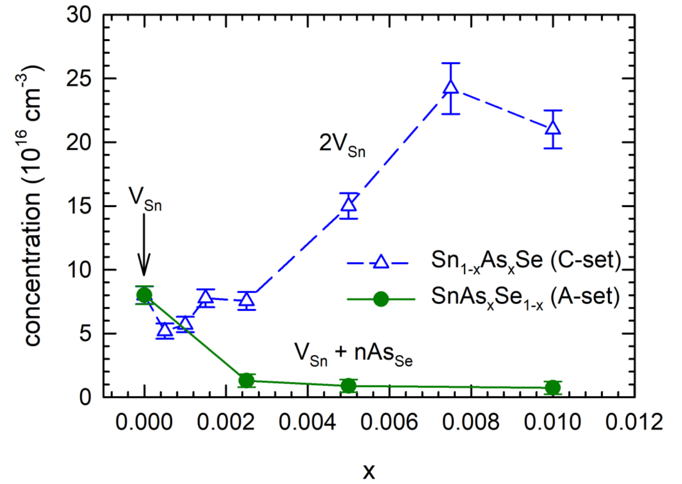

FIG. 8. The concentrations of point defects detected by LT spectroscopy in As-doped SnSe SCs plotted as a function of As content, namely V_{Sn} for $x = 0$, V_{Sn} complexes with As_{Se} for the A set ($x > 0$) and 2 V_{Sn} for the C set ($x > 0$).

The undoped sample ($x = 0$) exhibits a lifetime of $\tau_2 =$ 307 ps ($\tau/\tau_B = 1.41$) for trapped positrons, which agrees well with the lifetime ratio $\tau/\tau_B \approx 1.4$ calculated for V_{Sn}. Hence, undoped SnSe contains V_{Sn} as the dominant type of defect [13]. The development of vacancies significantly differs depending on whether As is a substitute for Se ions (A set) or Sn ions (C set).

For $SnAs_xSe_{1-x}$ (A set), As doping results in a remarkable decrease in the concentration of V_{Sn}. Although As atoms prefer to occupy Se sites, forming As_{Se} defects (as discussed below) slightly increases the formation energy of V_{Sn}, thus decreasing the concentration of this defect. The remaining small number of V_{Sn} are preferentially coordinated by As atoms. This process of coordinating V_{Sn} and As_{Se} defects is supported by coincidence Doppler broadening analysis [62]. The increase in LT τ_2 for $x = 0.01$ [see Fig. 5(a)] can be attributed to the formation of complexes of 2 V_{Sn}, which might be associated with As_{Se}. These complexes are characterized by positron lifetimes in the range of 315–317 ps. Note that V_{Se} can be excluded from possible intrinsic defects in $SnAs_xSe_{1-x}$ since theoretical calculations showed that this defect is characterized by a lifetime ratio $\tau/\tau_B \approx 1.3$, which is lower than the τ_2/τ_B measured in the experiment. Moreover, the lifetime of positrons trapped in V_{Se} strongly increases with increasing number of As ions surrounding V_{Se} (Fig. 7), which was not observed in the experiment.

For $Sn_{1-x}As_xSe$ (C set), in contrast, the concentration of positron traps increases with increasing As content. This is demonstrated in Fig. 6(b) by an increase in the intensity I_2 of the defect component with lifetime $\tau_2 \approx 320$ ps. This component can be attributed to positrons trapped at defects consisting of several V_{Sn}, most likely V_{Sn} divacancies. The lifetime τ_1 of the free-positron component shortens in accordance with the two-state positron simple trapping model [61]. The concentrations of the point defects [V_{Sn}] (for $x = 0$) and [$V_{Sn} + nAs_{Se}$] (A set) and [2 V_{Sn}] (C set) (for $x > 0$) determined from the LT data using STM are plotted in Fig. 8. Note that for small vacancy clusters consisting of n vacancies ($n < 10$), the positron trapping coefficient is proportional to the number of vacancies in the cluster [63]. Hence the trapping coefficient for 2 V_{Sn} was estimated to be $2\nu_v$. Inspection of Fig. 8 shows that the concentration of defects decreases with As content for the A set, while for the C set it increases. A closer inspection reveals that the concentration of defects decreases for both sets of samples for very low As concentration $x \leqslant 0.001$. Namely, we observe a drop in the concentration of V_{Sn} even for the C set ($Sn_{1-x}As_xSe$), where the preferential substitution of As for Se drives the crystal to Sn-poor composition. As discussed above, this result reflects that SnSe is not a strict daltonide but allows a small off-stoichiometry connected with rather high concentration of V_{Sn} [13]. Hence, we conclude that although the As preferential substitution for Se generally increases the formation energy of V_{Sn} (the concentration of this defect should decrease), the shift in the stoichiometry towards cation poor composition induces the formation of cation vacancies in the C set. Hence, even in the C set ($Sn_{1-x}As_xSe$), some fraction of As dopants substitutes Se, which creates conditions favorable for the formation of V_{Sn}. Such formation of V_{Sn} is, however, observed for higher concentrations of As only. In fact, the C-set samples should be viewed as $Sn_{1-x}(As, Se)_{1+x}$. In terms of this notation, the preferential substitution of As for Se explains the increasing concentration of V_{Sn} in the C set, as stated above.

Investigations of binary $Sn_{2-y}Se_y$ SCs confirmed that Sn-poor conditions lead to formation of V_{Sn}; see Figs. 2 and 3. A similar effect occurs also in the C set where some fraction of As dopants substitutes Se ions instead of Sn ones, leading to stoichiometric shift (Sn deficiency) due to As doping. In contrast to this, in the A set As dopants substitute almost exclusively Se ions and an unintentional shift in the stoichiometry plays a negligible role.

These conclusions are further supported by coincidence Doppler broadening. Figure 9 presents CDB ratio curves related to the Al reference for A set and C set. The high-momentum part (HMP) of the CDB ratio curves ($p >$ 10×10^{-3} m_0c) represents predominantly a contribution of

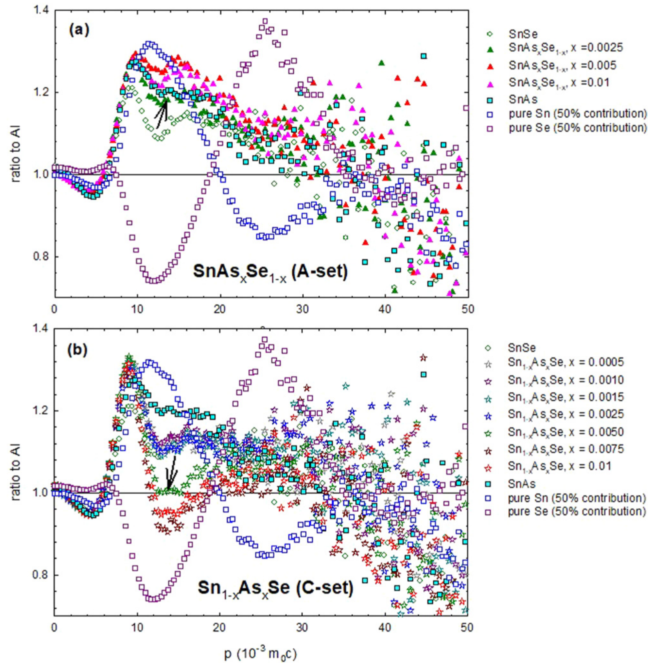

FIG. 9. CDB ratio curves (related to Al) for (a) $SnAs_xSe_{1-x}$ (*A* set) samples and (b) $Sn_{1-x}As_xSe$ (*C* set) samples. The figure contains also CDB ratio curves for pure Sn and Se elements reduced to 50% contribution. The CDB ratio curve for SnAs compound is plotted in the figure as well. The arrows show the tendency upon doping.

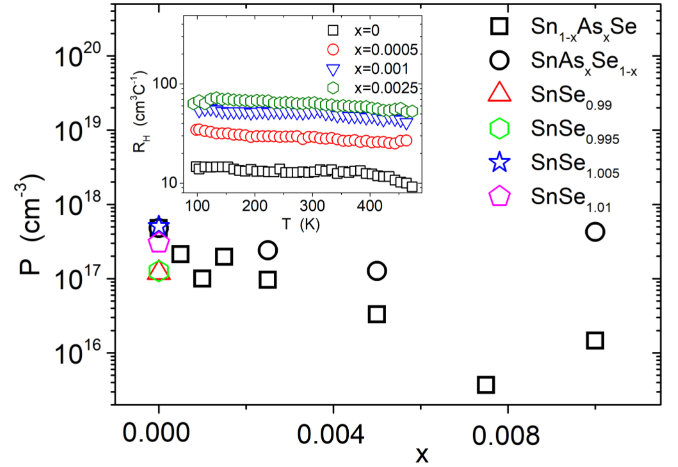

FIG. 10. The room-temperature Hall concentration P for As-doped SnSe SCs as a function of the As content, x and nonstoichiometric $Sn_{2-y}Se_y$ SCs. The Hall concentration $P = 1/R_H e$, where R_H is the Hall coefficient and e is the electron charge. The inset shows the Hall coefficient as a function of temperature for the four lowest concentrations of As for $Sn_{1-x}As_xSe$, the *C* set. The Hall concentration of nonstoichiometric samples is provided for comparison.

positrons annihilated by core electrons. Since the core electrons localized in the inner shells retain their atomic character and are almost not influenced by crystal bonding, the analysis of HMP provides information about local chemical environment of positron annihilation sites. For this reason, HMPs of the CDB spectra of the samples studied can be compared with the curves for reference samples of pure elements. The CDB ratio curves measured for reference samples of pure Sn and Se elements and reduced to 50% contribution are plotted in Fig. 9 as well. One can see that prominent feature of the Sn curve is a pronounced peak at $p \approx 11 \times 10^{-3}\ m_0c$ followed by a minimum at higher moments. The CDB curve for Se has luckily almost opposite shape with a peak at $p \approx 8 \times 10^{-3}\ m_0c$ followed by a minimum at $p \approx 12 \times 10^{-3}\ m_0c$ and a pronounced peak located at $p \approx 25 \times 10^{-3}\ m_0c$. The CDB ratio curve for SnSe SC exhibits a narrow peak at $p \approx 10 \times 10^{-3}\ m_0c$ followed by a local minimum at $p \approx 12.5 \times 10^{-3}\ m_0c$ and a second wider peak at $p \approx 17 \times 10^{-3}\ m_0c$. The shape of this curve in the high-momentum range can be understood considering superposition of contributions of positrons annihilated by electrons belonging to Sn and Se. More detailed description is given in Ref. [62]. Since a reference sample of pure As was not available (it is air- and moisture sensitive), stoichiometric SnAs compound was measured to get a hint about the shape of the momentum distribution of positrons annihilated by As electrons [64]. The ratio curve of SnAs sample is plotted in Fig. 9 as well and consists of a peak at $p \approx 10 \times 10^{-3}\ m_0c$ representing a contribution of positrons annihilated by Sn electrons and a broad shoulder in the momentum range 14–27 $\times 10^{-3}\ m_0c$, which comes predominantly from positrons annihilated by As electrons. Hence, the narrow peak at $p \approx 10 \times 10^{-3}\ m_0c$ is a measure of the contribution of positrons annihilated in the vicinity of Sn ions, while the shoulder in the high-momentum range 14–27 $\times 10^{-3}\ m_0c$ can be viewed as a measure of the contribution of positrons annihilated in the vicinity of Se or As ions. The CDB ratio curves of *A*-set ($SnAs_xSe_{1-x}$) samples increase in the high-momentum range with increasing As concentration and exhibit growing contribution of positrons annihilated in the vicinity of As ions; see Fig. 9(a). It indicates that the concentration of V_{Sn} decreases and that As ions are located preferentially in NN sites around V_{Sn}. On the other hand, *C*-set ($Sn_{1-x}As_xSe$) samples exhibit opposite behavior: The high-momentum contribution decreases with increasing As concentration and the ratio curves become "Se-like" with a pronounced minimum at $p \approx 13 \times 10^{-3}\ m_0c$; see Fig. 9(b). It indicates increasing concentration of open volume defects, namely V_{Sn}, which are surrounded by Se ions in NN sites. Hence, CDB results support the picture outlined by LT spectroscopy that *A*-set samples contain V_{Sn} associated with As_{Se} NNs, and their concentration decreases with increasing As content, while *C*-set samples contain V_{Sn} that are not coupled with As, and their concentration increases with the As content.

B. Transport properties

The Hall concentration (HC) of holes decreases with As doping, reaching very low room-temperature values, on the order of or even lower than $10^{16}\ cm^{-3}$ ($x = 0.0075$) for the *C* set (Fig. 10). In the *C* set, there is a local minimum in the HC at approximately $x = 0.001$ due to the interaction of As_{Se} with V_{Sn}. First, the concentration of V_{Sn} generally decreases upon As doping (although the concentration of this defect increases due to the shift in stoichiometry for $x > 0.001$ in the *C* set). This result is consistent with the conclusion drawn from PAS; cf. the discussion of Fig. 9(a). Second, the activation energy of V_{Sn} (although not measured as discussed below) increases

TABLE II. Room-temperature values for transport parameters of $Sn_{1-x}As_xSe$ single crystals. η denotes reduced Fermi level; please see Ref. [68] for details.

x	σ (Sm^{-1})	S (μVK^{-1})	η (−)	R_H ($cm^3\ C^{-1}$)	$P = 1/(R_He)$ ($10^{18}\ cm^{-3}$)	$\mu_H = R_H\sigma$ ($cm^2\ V^{-1}\ s^{-1}$)	$PF = \sigma S^2$ ($mW\ m^{-1}\ K^{-2}$)
0	1080	498	−3.8	13.1	0.477	141	0.268
0.0005	473	643	−5.5	29.4	0.212	139	0.196
0.001	21.4	680	−5.9	893	0.007	191	0.010
0.0015	182	661	−5.7	31.9	0.196	58	0.080
0.0025	115	705	−6.2	68.7	0.091	79	0.057
0.005	61.2	810	−7.4	190	0.033	116	0.040
0.0075	4.05	971	−9.3	1778	0.004	72	0.004
0.01	10.2	837	−7.8	598	0.010	61	0.007

evidently due to coupling with As_{Se} defects. Namely, 1.7 V_{Sn} are needed to produce one hole in undoped SnSe, while more than 11 V_{Sn} are necessary for the same effect in $Sn_{1-x}As_xSe$ for $x = 0.0025$. Furthermore, a comparison of Fig. 9(a) and Fig. 10 implies that any higher concentration of V_{Sn} for $x > 0.001$ in the C-set is not reflected in an associated increase in HC. Note that the local minimum of the HC at $x = 0.001$ (Fig. 10) coincides with the extrema in Figs. 5(b), 6(b), and 8. The Hall coefficient is almost temperature independent for all the samples, although a very small activation appears for the undoped sample above 400 K that can be attributed to V_{Sn}. The room-temperature values of the transport parameters are summarized in Table II.

It must be stressed that such a low concentration of holes as in the C set for $x = 0.0025$ is not achieved in undoped SnSe samples by any other means. We observe the lowest concentration of holes of $\approx 2 \times 10^{17}\ cm^{-3}$ at room temperature (RT) in an undoped stoichiometric sample that was cooled down from melt to room temperatures over 8 weeks to reach the room-temperature equilibrium state. Likewise, the same procedure including tuning the Sn/Se stoichiometry can decrease the RT concentration of holes to $\approx 8 \times 10^{16}\ cm^{-3}$ (for a composition of $SnSe_{0.99}$), which is connected with depletion of V_{Sn} [13].

Generally, As doping decreases the free-carrier (FC) mobility, $\mu(T)$ (Fig. 11), indicating the embedding of As atoms into the SnSe matrix, i.e., formation of point substitutional defects of As in place of Se (As_{Se}). The mobility of the undoped sample is comparable with published data [65]. The decrease in the Hall mobility is more pronounced in the C set for $x > 0.005$. This result is in accordance with conclusions drawn from PAS that the C set contains a much higher concentration of Sn vacancies. On the other hand, the mobility difference is not dramatic, which suggests that the effective scattering cross section of V_{Sn} is not large in comparison to As_{Se} (compare also with nonstoichiometric samples). In addition, As doping varies the scattering mechanism (inset of Fig. 11). While the $\mu(T)$ of the undoped sample follows scattering on acoustic phonons over the whole temperature range measured, the $\mu(T)$ of the As-doped samples indicates an admixture of other types of scattering on impurities (lower absolute slope in inset of Fig. 11) [66]. Thus, we observed an increase in the concentration of impurities, in accordance with PAS, but no increase in the FC concentration. This result implies that As_{Se} and the derived complexes are deep donors/acceptors with higher activation energy. Unfortunately, measurements at higher temperatures ($T > 500$ K) lead to hysteresis of the transport parameters upon temperature cycling, which interferes with the activation energy measurement. Note that although the FC mobility generally decreases upon As doping, this parameter exceeds the values for pure SnSe for $x \approx 0.001$ in the higher temperature region. Hence, the decrease in the scattering magnitude of native defects more than compensates for the increase in scattering due to As_{Se} defects in this case. This result suggests a healing process. In view of Ref. [13], this result could be important for optical or PV applications, where the native defects are related to nonstoichiometry and hence formation of extraneous phases that are detrimental to the efficiency of PV conversion [36]. Although the Hall mobility μ_H can differ markedly from the drift mobility μ for different Fermi levels or varying scattering mechanisms [67], the healing process is indisputable [68].

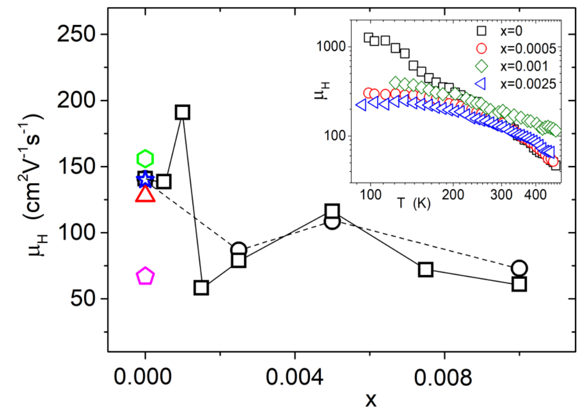

FIG. 11. The room-temperature Hall mobility $\mu_H = R_H\sigma$ for As-doped SnSe SCs as a function of the As content, x. R_H is the Hall coefficient, and σ is the electric conductivity. The Hall mobility of nonstoichiometric $Sn_{2-y}Se_y$ SCs is provided for comparison. Please use the legend of Fig. 10. The inset shows the Hall mobility as a function of temperature for the four lowest concentrations of As in C set.

IV. CONCLUSIONS

We can summarize the resulting picture as follows. $SnAs_xSe_{1-x}$ (*A* set): As atoms tend to substitute preferentially for Se atoms. The concentration of V_{Sn} decreases with As content by an order of magnitude, and around 80% of positrons annihilate in the free state for $x = 0.01$, indicating that As increases the formation energy of V_{Sn}. The remaining small number of V_{Sn} are preferentially coordinated with As atoms. Importantly, the Hall concentration decreases upon doping. A slight As substitution for Se clearly leads to healing of the host structure due to the removal of Sn vacancies. Thus, a very low concentration of As could be favorable for photovoltaic applications, where the occurrence of V_{Sn} is related to the formation of extraneous phases that are detrimental to the efficiency of PV conversion. The As-induced depletion of extraneous-phase $SnSe_2$ is corroborated by the high-resolution XRD in the *A* set [69]. However, the carrier mobility tends to decrease with As doping, generally indicating a structural disorder due to As substitution. $Sn_{1-x}As_xSe$ (*C* set): In contrast to the *A* set, the concentration of V_{Sn} markedly increases (Figs. 3 and 7) with As content, and the vacancies are coordinated preferentially with Se. The annihilation of positrons with As electrons is less evident, suggesting that As atoms partially coordinate with Sn vacancies only in the *A* set. As_{Se} is a deep defect that produces no FCs at room temperature. Correspondingly, the Hall concentration decreases upon doping and stays below 10^{16} cm^{-3} for $x = 0.0075$. In terms of TE, As doping is detrimental to both the TE efficiency and thermal stability.

Results presented in this paper indicate that doping of SnSe is a rather complex process that generally includes a strong interaction of doping atoms with the hosting structure. Such a strong interaction, on the other hand, indicates that doping could generally be used to adjust the type and concentration of defects. From this perspective, a high concentration of V_{Sn} or vacancy cluster defects might enable low-temperature TE application of SnSe. In terms of defect structure healing, further exploration of SnSe for photovoltaic applications is also worthwhile. However, the diverse interactions of defects with doping species that are temperature dependent generally impede any high-temperature applications of SnSe.

ACKNOWLEDGMENTS

We acknowledge the financial support from the Grant Agency of the Czech Republic (GA CR), Project No. 18-09347S (J.C.) and Project No. 19-16315S (J.N. and C.D.). V.H. acknowledges the support of the project NanoCent financed by European Regional Development Fund (ERDF, Project No. CZ.02.1.01/0.0/0.0/15.003/0000485).

[1] G. S. Nolas, J. Sharp, and H. J. Goldsmid, *Thermoelectrics, Basic Principles and New Materials Developments* (Springer, Berlin, 2001), p. 128.

[2] T. Plirdpring, K. Kurosaki, A. Kosuga, T. Day, S. Firdosy, V. Ravi, G. J. Snyder, A. Harnwunggmoung, T. Sugahara, Y. Ohishi, H. Muta, and S. Yamanaka, Chalcopyrite CuGaTe(2): A high-efficiency bulk thermoelectric material, Adv. Mater. **24**, 3622 (2012).

[3] R. Liu, L. Xi, H. Liu, X. Shi, W. Zhang, and L. Chen, Ternary compound CuInTe2: A promising thermoelectric material with diamond-like structure, Chem. Commun. **48**, 3818 (2012).

[4] S. Bhattacharya, R. Basu, R. Bhatt, S. Pitale, A. Singh, D. K. Aswal, S. K. Gupta, M. Navaneethan, and Y. Hayakawa, $CuCrSe_2$: A high performance phonon glass and electron crystal thermoelectric material, J. Mater. Chem. A **1**, 11289, (2013).

[5] L.-D. Zhao, S.-H. Lo, Y. Zhang, H. Sun, G. Tan, C. Uher, C. Wolverton, V. P. Dravid, and M. G. Kanatzidis, Ultralow thermal conductivity and high thermoelectric figure of merit in SnSe crystals, Nature (London) **508**, 373 (2014).

[6] S. Sassi, C. Candolfi, J.-B. Vaney, V. Ohordniichuk, P. Masschelein, A. Dausher, and B. Lenoir, Assessment of the thermoelectric performance of polycrystalline p-type SnSe, Appl. Phys. Lett. **104**, 212105 (2014).

[7] Y. K. Lee, Z. Luo, S. P. Cho, M. G. Kanatidis, and I. Chung, Surface oxide removal for polycrystalline SnSe reveals near-single-crystal thermoelectric performance, Joule **3**, 719 (2019).

[8] T. Chattopadhyay, J. Pannetier, and H. G. Von Schnering, Neutron diffraction study of the structural phase transition in SnS and SnSe, J. Phys. Chem. Solids **47**, 879 (1986).

[9] M. Sist, J. Zhang, and B. Brummerstedt Iversen, Crystal structure and phase transition of thermoelectric SnSe, Acta Crystallogr., Sect. B: Struct. Sci., Cryst. Eng. Mater. **72**, 310 (2016).

[10] K. Kurosaki, A. Kosuga, H. Muta, M. Uno, and S. Yamanaka, Ag_9TlTe_5: A high-performance thermoelectric bulk material with extremely low thermal conductivity, Appl. Phys. Lett. **87**, 061919 (2005).

[11] Rhyee, K. H. Lee, S. M. Lee, E. Cho, S. I. Kim, E. Lee, S. Y. Kwon, J. H. Shim, and G. Kotliar, Peierls distortion as a route to high thermoelectric performance in In(4)Se(3-delta) crystals, Nature (London) **459**, 965 (2009).

[12] Ch.-L. Chen, H. Wang, Y.-Y. Chen, T. Day, and G. J. Snyder, Thermoelectric properties of p-type polycrystalline SnSe doped with Ag, J. Mater. Chem. A **2**, 11171 (2014).

[13] K. Sraitrova, J. Cizek, V. Holy, T. Plechacek, L. Benes, M. Jarosova, V. Kucek, and C. Drasar, Vacancies in SnSe single crystals in a near-equilibrium state, Phys. Rev. B **99**, 035306 (2019).

[14] H. Leng, M. Zhou, J. Zhao, Y. Han, and L. Li, Optimization of thermoelectric performance of anisotropic $Ag_xSn_{1-x}Se$ compounds, J. Electron. Mater. **45**, 527 (2016).

[15] T.-R. Wei, G. Tan, X. Zhang, Ch.-F. Wu, J.-F. Li, V. P. Dravid, G. J. Snyder, and M. G. Kanatzidis, Distinct impact of alkali-ion doping on electrical transport properties of thermoelectric p-type polycrystalline SnSe, J. Am. Chem. Soc. **138**, 8875 (2016).

[16] L.-D. Zhao, G. Tan, S. Hao, J. He., Y. Pei, H. Chi, H. Wang, S. Gong, H. Xu, V. P. Dravid, C. Uher, G. F. Snyder, Ch. Wolverton, and M. G. Kanatzidis, Ultrahigh power factor and thermoelectric performance in hole-doped single-crystal SnSe, Science **351**, 141 (2016).

[17] H.-Q. Leng, M. Zhou, J. Zhao, Y.-M. Han, and L.-F. Li, The thermoelectric performance of anisotropic SnSe doped with Na, RSC Adv. **6**, 9112 (2016).
[18] B. Cai, J. Li, J. Sun, P. Zhao, F. Yu, L. Zhan, D. Yu, Y. Tian, and B. Xu, Sodium doped polycrystalline SnSe: High pressure synthesis and thermoelectric properties, J. Alloys Compd. **727**, 1014 (2017).
[19] Y.-X. Chen, Z.-H. Ge, M. Yin, D. Feng, X.-Q. Huang, W. Zhao, and J. He, Understanding of the extremely low thermal conductivity in high-performance polycrystalline SnSe through potassium doping, Adv. Funct. Mater. **26**, 6836 (2016).
[20] C.-C. Lin, D. Ginting, G. Kim, K. Ahn, and J.-S. Rhyee, High thermoelectric performance and low thermal conductivity in K-doped SnSe polycrystalline compounds, Curr. Appl. Phys. **18**, 1534 (2018).
[21] J. C. Li, D. Li, X. Y. Qin, and J. Zhang, Enhanced thermoelectric performance of p-type SnSe doped with Zn, Scr. Mater. **126**, 6 (2017).
[22] J. Gao and G. Xu, Thermoelectric performance of polycrystalline $Sn_{1-x}Cu_xSe$ ($x = 0$–0.03) prepared by high pressure method, Intermetallics **89**, 40 (2017).
[23] V. Kucek, T. Plechacek, P. Janicek, P. Ruleova, L. Benes, J. Navratil, and C. Drasar, Thermoelectric properties of Tl-doped SnSe: A hint of phononic structure, J. Electron. Mater. **45**, 2943 (2016).
[24] X. Shi, A. Wu, T. Fen, K. Zheng, W. Liu, Q. Sun, M. Hon, S. T. Pantelides, Z.-G. Chen, and J. Zou, High thermoelectric performance in p-type polycrystalline Cd-doped SnSe achieved by a combination of cation vacancies and localized lattice engineering, Adv. Energy Mater. **9**, 1803242 (2019).
[25] J. Yang, G. Zhang, G. Yang, C. Wang, and Y. X. Wang, Outstanding thermoelectric performances for both p-and n-type SnSe from first-principles study. J. Alloys Compd. **644**, 615 (2015).
[26] A. J. Hong, L. Li, H. X. Zhu, Z. B. Yan, J.-M. Liu, and Z. F. Ren, Optimizing the thermoelectric performance of low-temperature SnSe compounds by electronic structure design, J. Mater. Chem. A **3**, 13365 (2015).
[27] A. Dewandre, O. Hellman, S. Bhattacharya, A. H. Romero, G. K. H. Madsen, and M. J. Verstraete, Two-Step Phase Transition in SnSe and the Origins of its High Power Factor from First Principles, Phys. Rev. Lett. **117**, 276601 (2016).
[28] A. T. Duong, V. Q. Nguyen, G. Duvjir, V. T. Duong, S. Kwon, J. Y. Song, J. K. Lee, J. E. Lee, S. D. Park, T. Min, J. Lee, J. Kim, and S. Cho, Achieving ZT = 2.2 with Bi-doped n-type SnSe single crystals, Nat. Commun. **7**, 13713 (2016).
[29] S. Li, Y. Wang, Ch. Chen, X. Li, W. Xue, X. Wang, Z. Zhang, F. Cao, J. Sui, X. Liu, and Q. Zhang, Heavy doping by bromine to improve the thermoelectric properties of n-type polycrystalline SnSe, Adv. Sci. **5**, 1800598 (2018).
[30] W. Wei, Ch. Chang, T. Yang, J. Liu, H. Tang, J. Zhang, Y. Li, F. Xu, Z. Zhang, J.-F. Li, and G. Tang, Achieving high thermoelectric figure of merit in polycrystalline SnSe via introducing Sn vacancies, J. Am. Chem. Soc. **140**, 499 (2018).
[31] D. Wu, L. Wu, D. He, L.-D. Zhao, W. Li, M. Wu, M. Jin, J. Xu, J. Jiang, L. Huang, Y. Zhu, M. G. Kanatzidis, and J. He, Direct observation of vast off-stoichiometric defects in single crystalline SnSe, Nano Energy **35**, 321 (2017).
[32] Y. Huang, Ch. Wang, X. Chen, D. Zhou, J. Du, S. Wang, and L. Ning, First-principles study on intrinsic defects of SnSe, RSC Adv. **7**, 27612 (2017).
[33] J. Vidal, S. Lany, M. d'Avezac, A. Zunger, A. Zakutayev, J. Francis, and J. Tate, Band-structure, optical properties, and defect physics of the photovoltaic semiconductor SnS, Appl. Phys. Lett. **100**, 032104 (2012).
[34] J. Navrátil, K. Šraitrová, V. Kucek, T. Plecháček, J. Kašparová, and Č. Drašar, Investigation of an amphoteric behavior of arsenic dopant in polycrystalline SnSe, Sci. Pap. Univ. Pardubice, Ser. A **24**, 87 (2018).
[35] L. A. Burton and A. Walsh, Phase stability of the earth-abundant tin sulfides SnS, SnS_2, and Sn_2S_3, J. Phys. Chem. C **116**, 24262 (2012).
[36] L. A. Burton, D. Colombara, R. D. Abellon, F. C. Grozema, L. M. Peter, T. J. Savenije, G. Dennler, and A. Walsh, Synthesis, characterization, and electronic structure of single-crystal SnS, Sn_2S_3, and SnS_2, Chem. Mater. **25**, 4908 (2013).
[37] https://www.ill.eu/sites/fullprof/.
[38] See Supplemental Material at http://link.aps.org/supplemental/10.1103/PhysRevB.103.085203 for details of the XRD and inductively coupled plasma optical emission spectrometry measurements and results.
[39] R. Krause-Rehberg and H. Leipner, *Positron Annihilation in Semiconductors* (Springer-Verlag, Berlin, 1999).
[40] P. Asoka-Kumar, M. Alatalo, V. J. Ghosh, A. C. Kruseman, B. Nielsen, and K. G. Lynn, Increased Elemental Specificity of Positron Annihilation Spectra, Phys. Rev. Lett. **77**, 2097 (1996).
[41] F. Becvar, J. Cizek, I. Prochazka, and J. Janotova, The asset of ultra-fast digitizers for positron-lifetime spectroscopy, Nucl. Instrum. Methods Phys. Res., Sect. A **539**, 372 (2005).
[42] I. Prochazka, I. Novotny, and F. Becvar, Application of maximum-likelihood method to decomposition of positronlifetime spectra to finite number of components, Mater. Sci. Forum. **255-257**, 772 (1997).
[43] H. Surbeck, Lebensdauer der positronen in silberbromid, Helv. Phys. Acta **50**, 705 (1977).
[44] J. Cizek, M. Vlcek, and I. Prochazka, Digital spectrometer for coincidence measurement of Doppler broadening of positron annihilation radiation, Nucl. Instrum. Methods Phys. Res., Sect. A **623**, 982 (2010).
[45] M. J. Puska and R. M. Nieminen, Defect spectroscopy with positrons: A general calculational method, J. Phys. F Met. Phys. **13**, 333 (1983).
[46] M. J. Puska and R. M. Nieminen, Theory of positrons in solids and on solid surfaces, Rev. Mod. Phys. **66**, 841 (1994).
[47] J. P. Desclaux, Hartree Fock Slater self consistent field calculation, Comput. Phys. Comm. **1**, 216 (1969).
[48] J. P. Desclaux, A multiconfiguration relativistic Dirac-Fock program, Comput. Phys. Comm. **9**, 31 (1975).
[49] A. P. Seitsonen, M. J. Puska, and R. M. Nieminen, Real-space electronic-structure calculations: Combination of the finite-difference and conjugate-gradient methods, Phys. Rev. B **51**, 14057 (1995).
[50] E. Boronski and R. M. Nieminen, Electron-positron density-functional theory, Phys. Rev. B **34**, 3820 (1986).
[51] M. J. Puska, S. Mäkinen, M. Manninen, and R. M. Nieminen, Screening of positrons in semiconductors and insulators, Phys. Rev. B **39**, 7666 (1989).

[52] H. R. Chandrasekhar, R. G. Humphreys, U. Zwick, and M. Cardona, Infrared and Raman spectra of the IV-VI compounds SnS and SnSe, Phys. Rev. B **15**, 2177 (1977).

[53] B. Barbiellini, M. J. Puska, T. Korhonen, A. Harju, T. Torsti, and R. M. Nieminen, Calculation of positron states and annihilation in solids: A density-gradient-correction scheme, Phys. Rev. B **53**, 16201 (1996).

[54] T. Korhonen, M. J. Puska, and R. M. Nieminen, First-principles calculation of positron annihilation characteristics at metal vacancies, Phys. Rev. B **54**, 15016 (1996).

[55] M. Alatalo, B. Barbiellini, M. Hakala, H. Kauppinen, T. Korhonen, M. J. Puska, K. Saarinen, P. Hautojärvi, and R. M. Nieminen, Theoretical and experimental study of positron annihilation with core electrons in solids, Phys. Rev. B **54**, 2397 (1996).

[56] J. Kuriplach, A. L. Morales, C. Dauwe, D. Segers, and M. Sob, Vacancies and vacancy-oxygen complexes in silicon: Positron annihilation with core electrons, Phys. Rev. B **58**, 10475 (1998).

[57] H. Wiedemeier and F. J. Csillag, The thermal expansion and high temperature transformation of SnS and SnSe, Z. für Kristallogr. **149**, 17 (1979).

[58] K. Adouby, C. Perez-Vicente, J. C. Jumas, R. Fourcade, and A. A. Toure, Structure and temperature transformation of SnSe. stabilization of a new cubic phase $Sn_4Bi_2Se_7$, Z. für Kristallogr. **213**, 343 (1998).

[59] I. Makkonen, M. Hakala, and M. J. Puska, Modeling the momentum distributions of annihilating electron-positron pairs in solids, Phys. Rev. B **73**, 035103 (2006).

[60] G. Brauer, W. Anwand, D. Grambole, J. Grenzer, W. Skorupa, J. Čížek, J. Kuriplach, I. Procházka, C. C. Ling, C. K. So, D. Schulz, and D. Klimm, Identification of Zn-vacancy–hydrogen complexes in ZnO single crystals: A challenge to positron annihilation spectroscopy, Phys. Rev. B **79**, 115212 (2009).

[61] R. N. West, Positron studies of condensed matter, Adv. Phys. **22**, 263 (1973).

[62] See Supplemental Material at http://link.aps.org/supplemental/10.1103/PhysRevB.103.085203 for more results and discussion of the coincidence Doppler broadening measurement.

[63] R. M. Nieminen and J. Laakkonen, Positron trapping rate into vacancy clusters, Appl. Phys. **20**, 181 (1979).

[64] Y. Wang, H. Sato, Y. Toda, S. Ueda, H. Hiramatsu, and H. Hosono, SnAs with the NaCl-type structure: Type-I superconductivity and single valence state of Sn, Chem. Mater. **26**, 7209 (2014).

[65] Z. Wang, C. Fan, Z. Shen, Ch. Hua, Q. Hu, F. Sheng, Y. Lu, H. Fang, Z. Qiu, J. Lu, Z. Liu, W. Liu, Y. Huang, Z.-A. Xu, D. W. Shen, and Y. Zheng, Defects controlled hole doping and multivalley transport in SnSe single crystals, Nat. Commun. **9**, 47 (2018).

[66] P. Cermak, P. Knotek, P. Ruleova, V. Holy, K. Palka, V. Kucek, L. Benes, J. Navratil, and C. Drasar, High power factor and mobility of single crystals of Bi2Se3 induced by Mo doping, J. Solid State Chem. **277**, 819 (2019).

[67] V. I. Fistul, *Heavily Doped Semiconductors* (Springer, Boston, 1969), p. 108–125.

[68] See Supplemental Material at http://link.aps.org/supplemental/10.1103/PhysRevB.103.085203 for further Hall mobility discussion.

[69] See Supplemental Material at http://link.aps.org/supplemental/10.1103/PhysRevB.103.085203 for high-resolution x-ray diffraction results.